

Binary black hole spins: model selection with GWTC-3

Carole Périgois^{1,2,*}, Michela Mapelli^{1,2,3,†}, Filippo Santoliquido^{1,2,3}, Yann Bouffanais^{1,2}, and Roberta Rufolo¹.

¹Physics and Astronomy Department Galileo Galilei, University of Padova, Vicolo dell'Osservatorio 3, I-35122, Padova, Italy

²INFN - Padova, Via Marzolo 8, I-35131 Padova, Italy

³INAF - Osservatorio Astronomico di Padova, Vicolo dell'Osservatorio 5, I-35122 Padova, Italy

Accepted XXX. Received YYY; in original form ZZZ

ABSTRACT

The origin of the spins of stellar-mass black holes is still controversial, and angular momentum transport inside massive stars is one of the main sources of uncertainty. Here, we apply hierarchical Bayesian inference to derive constraints on spin models from the 59 most confident binary black hole merger events in the third gravitational-wave transient catalogue (GWTC-3). We consider up to five parameters: chirp mass, mass ratio, redshift, effective spin, and precessing spin. For model selection, we use a set of binary population synthesis simulations spanning drastically different assumptions for black hole spins and natal kicks. In particular, our spin models range from maximal to minimal efficiency of angular momentum transport in stars. We find that, if we include the precessing spin parameter into our analysis, models predicting only vanishingly small spins are in tension with GWTC-3 data. On the other hand, models in which most spins are vanishingly small, but that also include a sub-population of tidally spun-up black holes are a good match to the data. Our results show that the precessing spin parameter has a crucial impact on model selection.

Key words: black hole physics – gravitational waves – binaries: general – stars: black holes

1 INTRODUCTION

The third observing run (O3) of the Advanced LIGO (Aasi et al. 2015) and Virgo (Acernese et al. 2015) detectors has brought the number of compact binary merger observations up to 90 events with a probability of astrophysical origin > 0.5 (Abbott et al. 2019, 2021d,a,b). In particular, the 63 confident detections of binary black hole (BBH) mergers (with a false alarm rate $\text{FAR} < 0.25 \text{ yr}^{-1}$) lead to more accurate constraints on the mass and spin distribution of these systems (Abbott et al. 2021c).

The intrinsic distribution of primary black hole (BH) masses inferred by the LIGO–Virgo–KAGRA collaboration (hereafter, LVK) shows several sub-structures, including a main peak at $\approx 10 M_{\odot}$, a secondary peak at $\approx 30 - 40 M_{\odot}$, and a long tail extending up to $\sim 80 M_{\odot}$ (e.g., Abbott et al. 2021c). The inferred distribution of mass ratios has a strong preference for equal-mass systems, but several BBHs are confidently unequal-mass (e.g., GW190412 Abbott et al. 2020), (GW190517 Abbott et al. 2021d). Focusing on BH spins, we can safely exclude that all BHs are maximally spinning (Farr et al. 2017, 2018; Abbott et al. 2019). Typical spin magnitudes in BBHs are small, with $\sim 50\%$ of BHs having $\chi \lesssim 0.3$ (e.g., Wysocki et al. 2019; Abbott et al. 2021d), although not all BHs in the LVK sample have zero spin (Roulet & Zaldarriaga 2019; Miller et al. 2020). For example, GW151226 (Abbott et al. 2016a) and GW190517 (Abbott et al. 2021c) confidently possess spin. LVK data also support some mild evidence for spin-orbit misalignment (e.g., Tiwari et al. 2018;

Abbott et al. 2021d,c; Venumadhav et al. 2020; Olsen et al. 2022; Callister et al. 2021; Hannam et al. 2022; Callister et al. 2022).

These results provide crucial insights to understand BBH formation and evolution (e.g., Gerosa et al. 2013; Stevenson et al. 2015; Rodriguez et al. 2016; Stevenson et al. 2017; Talbot & Thrane 2017; Fishbach & Holz 2017; Vitale et al. 2017; Zevin et al. 2017; Farr et al. 2018; Barrett et al. 2018; Taylor & Gerosa 2018; Fragione & Kocsis 2020; Arca Sedda & Benacquista 2019; Roulet & Zaldarriaga 2019; Wysocki et al. 2019; Bouffanais et al. 2019, 2021a,b; Kimball et al. 2021; Kimball et al. 2020; Baibhav et al. 2020; Arca Sedda et al. 2020; Zevin et al. 2021; Mapelli et al. 2021, 2022). Moreover, the mass and spin of BHs carry the memory of their progenitor stars and therefore are a key to unravel the details of massive star evolution and collapse (e.g., Fryer & Kalogera 2001; Heger et al. 2003; Belczynski et al. 2010; Mapelli et al. 2013; Fragos & McClintock 2015; Marchant et al. 2016; Eldridge & Stanway 2016; de Mink & Mandel 2016; Spera & Mapelli 2017; Bavera et al. 2020; Belczynski et al. 2020; Fragione et al. 2022; Mandel et al. 2021; Fryer et al. 2022; Olejak et al. 2022; Chattopadhyay et al. 2022; van Son et al. 2022; Briel et al. 2022; Stevenson & Clarke 2022; Broekgaarden et al. 2022a,b). In particular, the spin magnitude of a stellar-origin BH should retain the imprint of the spin of the core of its progenitor star (e.g., Qin et al. 2018, 2019; Fuller & Ma 2019; Bavera et al. 2020; Belczynski et al. 2020; Olejak & Belczynski 2021; Stevenson 2022).

Several models have been proposed to infer the spin magnitude of the BH from that of the progenitor star. The main open question concerns the efficiency of angular momentum transport within a star (e.g., Maeder & Meynet 2000; Cantiello et al. 2014; Fuller et al.

* E-mail: caroleperigois@outlook.com (CP)

† E-mail: michela.mapelli@unipd.it

2019). If angular momentum is efficiently transferred from the core to the outer layers, mass loss by stellar winds can dissipate most of it, leading to a low-spinning stellar core and then to a low-spinning BH. If instead the core retains most of its initial angular momentum until the final collapse, the BH will be fast spinning.

In the shellular model (Zahn 1992; Ekström et al. 2012; Limongi & Chieffi 2018; Costa et al. 2019), angular momentum is mainly transported by meridional currents and shear instabilities, leading to relatively inefficient spin dissipation. In contrast, according to the Tayler-Spruit dynamo mechanism (Spruit 2002), differential rotation induces the formation of an unstable magnetic field configuration, leading to an efficient transport of angular momentum via magnetic torques. Building upon the Tayler-Spruit mechanism, Fuller & Ma (2019) derived a new model with an even more efficient angular momentum dissipation, predicting that the core of a single massive star might end its life with almost no rotation.

Electromagnetic observations yield controversial results. Asteroseismology favours slowly rotating cores in the late evolutionary stages, but the vast majority of stars with an asteroseismic estimate of the spin are low-mass stars (Mosser et al. 2012; Gehan et al. 2018; Aerts et al. 2019). Continuum-fitting derived spins of BHs in high-mass X-ray binaries are extremely high (e.g., Reynolds 2021; Miller-Jones et al. 2021; Fishbach & Kalogera 2022), but such measurements might be affected by substantial observational biases (e.g., Reynolds 2021). Finally, BH spins inferred from quasi-periodic oscillations yield notably smaller values than continuum fitting. For example, the estimate of the dimensionless spin of the BH in GRO J1655–40 is $\chi = 0.7 \pm 0.1$ and 0.290 ± 0.003 from continuum fitting (Shafee et al. 2006) and quasi-periodic oscillations (Motta et al. 2014), respectively.

In a binary system, the evolution of the spin is further affected by tidal forces and accretion, which tend to spin up a massive star, whereas non-conservative mass transfer and common-envelope ejection enhance mass loss, leading to more efficient spin dissipation (Kushnir et al. 2016; Hotokezaka & Piran 2017; Zaldarriaga et al. 2018; Qin et al. 2018). For example, the model by Bavera et al. (2020) shows that the second-born BH can be highly spinning if its progenitor was tidally spin up when it was a Wolf-Rayet star orbiting about the first-born BH.

Furthermore, the orientation of the BH spin with respect to the orbital angular momentum of the binary system encodes information about binary evolution processes. In a tight binary system, tides and mass transfer tend to align the stellar spins with the orbital angular momentum (Gerosa et al. 2018, but see Stegmann & Antonini 2021 for a possible spin flip process induced by mass transfer). If the binary system is in the field, the supernova kick is the main mechanism that can misalign the spin of a compact object with respect to the orbital angular momentum, by tilting the orbital plane (e.g., Kalogera 2000). Finally, the spins of BHs in dynamically formed binary systems are expected to be isotropically distributed, because close encounters in a dense stellar cluster reset any previous signature of alignment (e.g., Rodriguez et al. 2016; Mapelli et al. 2021).

Here, we perform a model-selection hierarchical Bayesian analysis on confident LVK BBHs ($p_{\text{astro}} > 0.9$ and $\text{FAR} < 0.25 \text{ yr}^{-1}$). We consider models of field BBHs for three of the most used angular-momentum transport models: (i) the shellular model as implemented in the Geneva stellar evolution code (Ekström et al. 2012), (ii) the Tayler-Spruit dynamo model as implemented in the MESA code (Cantiello et al. 2014), and (iii) the model by Fuller & Ma (2019). Hereafter, we will refer to these three models simply as GENEVA (G), MESA (M) and FULLER (F) models, following the description in Belczynski et al. (2020).

For each of these models, we consider an additional variation accounting for the Wolf-Rayet (WR) star tidal spin-up mechanism described by Bavera et al. (2020). Also, we account for spin tilts induced by core-collapse supernova explosions.

This paper is organized as follows. Section 2 presents our population-synthesis models. Section 3 describes the hierarchical Bayesian framework we used and discusses the LVK events used in our study. We lay down the results in Section 4, and summarize our conclusions in Section 5.

2 ASTROPHYSICAL MODELS

2.1 MOBSE and natal kicks

We simulated our binary systems with the code MOBSE (Mapelli et al. 2017; Giacobbo et al. 2018). MOBSE is a custom and upgraded version of BSE (Hurley et al. 2000, 2002), in which we introduced metallicity-dependent stellar winds for OB (Vink et al. 2001), WR (Belczynski et al. 2010), and luminous blue variable stars (Giacobbo & Mapelli 2018). MOBSE includes a formalism for electron-capture (Giacobbo & Mapelli 2019), core-collapse (Fryer et al. 2012), and (pulsational) pair-instability supernovae (Mapelli et al. 2020). Here, we adopt the rapid core-collapse supernova prescription, which enforces a gap between the maximum mass of neutron stars and the minimum mass of BHs (2–5 M_{\odot} , Özel et al. 2010; Farr et al. 2011).

We model natal kicks of neutron stars and BHs according to three different models, as shown in Fig. 1:

- A unified kick model, in which both neutron stars and BHs receive a kick $v_{\text{kick}} \propto m_{\text{ej}}/m_{\text{rem}}$, where m_{ej} is the mass of the ejecta and m_{rem} the mass of the compact remnant (Giacobbo & Mapelli 2020, hereafter GM20). This model naturally produces low-kicks for electron-capture, stripped and ultra-stripped supernovae (Tauris et al. 2015, 2017). Hereafter, we call this model GM20.
- A model in which compact-object kicks are drawn from a Maxwellian curve with one-dimensional root-mean-square $\sigma = 265 \text{ km s}^{-1}$, consistent with observations of Galactic pulsars (Hobbs et al. 2005). This realistically represents the upper limit for BH natal kicks. Hereafter, we name this model $\sigma 265$.
- A model in which compact-object kicks are drawn from a Maxwellian curve with $\sigma = 150 \text{ km s}^{-1}$. This value of σ is more similar to what suggested from indirect measurements of Galactic BH kicks (e.g., Repetto et al. 2017; Atri et al. 2019). Hereafter, we refer to this model as $\sigma 150$.

For more details about MOBSE, see Giacobbo & Mapelli (2018). MOBSE is an open-source code and can be downloaded from [this link](#).

2.2 Spin magnitude

We have implemented four models for the spin magnitude in MOBSE, the first three from Belczynski et al. (2020), and the fourth from Bouffanais et al. (2019). Given the large uncertainties on angular momentum transport, we do not claim that these four models are a complete description of the underlying physics: our models must be regarded as toy models, which bracket the current uncertainties on BH spins.

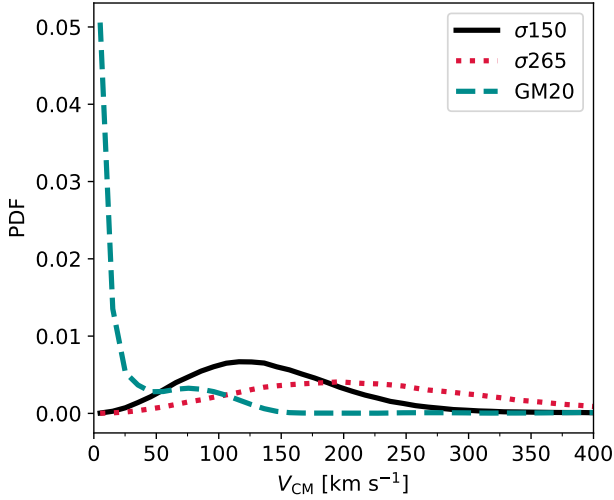


Figure 1. Probability distribution function (PDF) of the binary kick velocities in the centre of mass (V_{CM}), for our sample of simulated BBH mergers. The centre-of-mass kick velocity takes into account both the first and the second supernova event in each binary system (Perna et al. 2022). Dashed dark-cyan line: model GM20; solid black line: σ_{150} ; dotted red line: σ_{265} . This figure only shows the kick velocity of the stellar progenitors of BBHs that merge within the lifetime of the Universe.

b	m_1 (M_{\odot})	m_2 (M_{\odot})	a_{low}	Z
2.258	16.0	24.2	0.13	≥ 0.010
3.578	31.0	37.8	0.25	[0.004, 0.010]
2.434	18.0	27.7	0.0	[0.0012, 0.004]
3.666	32.0	38.8	0.25	< 0.0012

Table 1. Parameters adopted in model G. See Eq. 1 for details.

2.2.1 Geneva (G) model

In the Geneva (hereafter, G) model, the dimensionless natal spin magnitude of a BH (χ) can be approximated as:

$$\chi = \begin{cases} 0.85 & M_{\text{CO}} \leq m_1 \\ a M_{\text{CO}} + b & m_1 < M_{\text{CO}} < m_2 \\ a_{\text{low}} & M_{\text{CO}} \geq m_2 \end{cases} \quad (1)$$

where $a = -0.088$ for all models, M_{CO} is the final carbon-oxygen mass of the progenitor star, while the values of b , m_1 , m_2 , and a_{low} depend on metallicity, as indicated in Table 1. This model springs from a fit by Belczynski et al. (2020) to some evolutionary tracks by the Geneva group (Ekström et al. 2012), in which angular momentum transport is relatively inefficient.

2.2.2 MESA (M) model

In the M model, we use the fits done by Belczynski et al. (2020) to a set of stellar tracks run with the MESA code. MESA models the transport of angular momentum according to the Tayler-Spruit magnetic dynamo (Spruit 2002, see also Cantiello et al. 2014). This yields a dimensionless natal BH spin

$$\chi = \begin{cases} a_1 M_{\text{CO}} + b_1 & \text{if } M_{\text{CO}} \leq m_1 \\ a_2 M_{\text{CO}} + b_2 & \text{if } M_{\text{CO}} > m_1, \end{cases} \quad (2)$$

a_1	b_1	a_2	b_2	m_1 (M_{\odot})	Z
-0.0016	0.115	-	-	∞	≥ 0.010
-0.0006	0.105	-	-	∞	[0.004, 0.010]
0.0076	0.050	-0.0019	0.165	12.09	[0.0012, 0.004]
-0.0010	0.125	-	-	∞	≤ 0.0012

Table 2. Parameters adopted in model M. See Eq. 2 for details.

where a_1 , b_1 , and m_1 are given in Table 2.

2.2.3 Fuller (F) model

Fuller & Ma (2019) predict that angular momentum transport can be even more efficient than the one predicted by the Tayler-Spruit dynamo. Belczynski et al. (2020) summarize the results of the model by Fuller & Ma (2019) simply as $\chi = 0.01$ for all single stars and metallicities.

2.2.4 Maxwellian model (Max)

Finally, we also introduce a toy model in which we represent the spin of a BH as a random number drawn from a Maxwellian curve with one-dimensional root-means square $\sigma_{\chi} = 0.1$ and truncated to $\chi_{\text{max}} = 1.0$. This model has been first introduced by Bouffanais et al. (2019), because it is a good match to the distribution arising from LVK data (e.g., Abbott et al. 2019, 2021d,c). Hereafter, we will indicate this Maxwellian toy model as Max, for brevity.

2.3 Tidal spin up

The progenitor star of the second-born BH can be substantially spun-up by tidal interactions. In the scenario explored by Bavera et al. (2020), a common-envelope or an efficient stable mass transfer episode can lead to the formation of a BH–WR binary system, in which the WR star is the result of mass stripping. The orbital period of this BH–WR binary system can be sufficiently short to lead to efficient tidal synchronisation and spin-orbit coupling. The WR star is then efficiently spun-up. If the WR star then collapses to a BH directly, the final spin of the BH will retain the imprint of the final WR spin.

Based on the simulations by Bavera et al. (2020), Bavera et al. (2021) derive a fitting formula to describe the spin-up of the WR star and the final spin of the second-born BH:

$$\chi = \begin{cases} \alpha_{\text{WR}} \log_{10}^2(P/[\text{day}]) + \beta_{\text{WR}} \log_{10}(P/\text{day}) & \text{if } P \leq 1 \text{ d} \\ 0 & \text{otherwise,} \end{cases} \quad (3)$$

where P is the orbital period of the BH–WR system, $\alpha_{\text{WR}} = f(M_{\text{WR}}, c_1^{\alpha}, c_2^{\alpha}, c_3^{\alpha})$ and $\beta_{\text{WR}} = f(M_{\text{WR}}, c_1^{\beta}, c_2^{\beta}, c_3^{\beta})$. In this definition,

$$f(M_{\text{WR}}, c_1, c_2, c_3) = \frac{-c_1}{c_2 + \exp(-c_3 M_{\text{WR}}/[M_{\odot}])}, \quad (4)$$

where M_{WR} is the mass of the WR star, while the coefficients c_1 , c_2 and c_3 have been determined through non-linear least-square minimization and can be found in Bavera et al. (2021).

In MOBSE, we can use these fits for the spin of the second-born BH, while still adopting one of the models presented in the previous subsections (G, M, F, and Max) for the first-born BH.

Model Name	Spin Magnitude ^a	B21 ^b	Kick Model ^c
G	Geneva (G)	no	GM20, σ 265, σ 150
G_B21	Geneva (G)	yes	GM20, σ 265, σ 150
M	MESA (M)	no	GM20, σ 265, σ 150
M_B21	MESA (M)	yes	GM20, σ 265, σ 150
F	Fuller (F)	no	GM20, σ 265, σ 150
F_B21	Fuller (F)	yes	GM20, σ 265, σ 150
Max	Maxwellian (Max)	no	GM20, σ 265, σ 150
Max_B21	Maxwellian (Max)	yes	GM20, σ 265, σ 150

Table 3. Description of the runs performed for this work. ^aModel for the spin magnitude (Section 2.2). ^bCorrection of the spin magnitude accounting for tidal spin up, as described in B21 (Section 2.3). ^cModel for the natal kick (Section 2.1).

2.4 Spin orientation

We assume that natal kicks are the only source of misalignment between the orbital angular momentum vector of the binary system and the direction of BH spins (Rodríguez et al. 2016; Gerosa et al. 2018). Furthermore, we conservatively assume that accretion onto the first-born BH cannot change the direction of its spin (Maccarone et al. 2007). For simplicity, we also neglect the spin-flip process recently described by (Stegmann & Antonini 2021). Under such assumptions, we can derive the angle between the direction of the spins of the two compact objects and that of the orbital angular momentum of the binary system as (Gerosa et al. 2013; Rodríguez et al. 2016)

$$\cos \delta = \cos(\nu_1) \cos(\nu_2) + \sin(\nu_1) \sin(\nu_2) \cos(\phi), \quad (5)$$

where ν_i is the angle between the new (\vec{L}_{new}) and the old (\vec{L}_{old}) orbital angular momentum after a supernova ($i = 1, 2$ corresponding to the first and second supernova), so that $\cos(\nu) = \vec{L}_{\text{new}} \cdot \vec{L}_{\text{old}} / (L_{\text{new}} L_{\text{old}})$, while ϕ is the phase of the projection of the orbital angular momentum into the orbital plane.

2.5 Setup of MOBSE runs

Hereafter, we consider eight possible models for the spins (see also Table 3):

- the first four models (hereafter, G, M, F, and Max) adopt the Geneva, Mesa, Fuller and Maxwellian models for both the first- and second-born BHs,
- the other four models (hereafter, G_B21, M_B21, F_B21, and Max_B21) adopt the fits by Bavera et al. (2021) for the second-born BH and the Geneva, Mesa, Fuller and Maxwellian models for the first-born BH.

For each of these eight spin models we consider three different kick models: the GM20, σ 265, and σ 150 models discussed in Section 2.1.

Finally, for each of these 24 models, we considered 12 metallicities ($Z = 0.0002, 0.0004, 0.0008, 0.0012, 0.0016, 0.002, 0.004, 0.006, 0.008, 0.012, 0.016, \text{ and } 0.02$). For each metallicity, we ran 10^7 (2×10^7) binary systems if $Z \leq 0.002$ ($Z \geq 0.004$). Hence, for each model we ran 1.8×10^8 binary systems, for a total of 4.32×10^9 binary systems encompassing the eight models.

We sampled the initial conditions for each binary system as follows. We have randomly drawn the zero-age main sequence mass of the primary stars from a Kroupa (Kroupa 2001) initial mass function in the range $5 - 150 M_{\odot}$. The initial orbital parameters (semi-major axis, orbital eccentricity and mass ratio) of binary stars have been randomly drawn as already described in Santoliquido et al.

(2021). In particular, we derive the mass ratios $q \equiv m_2/m_1$ (with $m_2 \leq m_1$) as $\mathcal{F}(q) \propto q^{-0.1}$ with $q \in [0.1, 1]$, the orbital period P from $\mathcal{F}(\Pi) \propto -0.55$ with $\Pi = \log_{10}(P/d) \in [0.15, 5.5]$ and the eccentricity e from $\mathcal{F}(e) \propto e^{-0.42}$ with $0 \leq e \leq 0.9$ (Sana et al. 2012).

As to the main binary evolution parameters, here we use $\alpha = 1$ for common envelope, while the parameter λ depends on the stellar structure as described in Claeys et al. (2014). The other binary evolution parameters are set-up as described in Santoliquido et al. (2021).

2.6 Merger rate density

We estimate the evolution of BBH mergers with redshift by using our semi-analytic code COSMORATE (Santoliquido et al. 2020, 2021). With COSMORATE, we convolve our MOBSE catalogues (Section 2.5) with an observation-based metallicity-dependent star formation rate (SFR) density evolution of the Universe, SFRD(z, Z), in order to estimate the merger rate density of BBHs as

$$\mathcal{R}_{\text{BBH}}(z) = \int_{z_{\text{max}}}^z \left[\int_{Z_{\text{min}}}^{Z_{\text{max}}} \text{SFRD}(z', Z) \mathcal{F}(z', z, Z) dZ \right] \frac{dt(z')}{dz'} dz', \quad (6)$$

where

$$\frac{dt(z')}{dz'} = [H_0 (1 + z')]^{-1} [(1 + z')^3 \Omega_M + \Omega_{\Lambda}]^{-1/2}. \quad (7)$$

In the above equation, H_0 is the Hubble constant, Ω_M and Ω_{Λ} are the matter and energy density, respectively. We adopt the values in Aghanim et al. (2020). The term $\mathcal{F}(z', z, Z)$ is given by:

$$\mathcal{F}(z', z, Z) = \frac{1}{\mathcal{M}_{\text{TOT}}(Z)} \frac{dN(z', z, Z)}{dt(z)}, \quad (8)$$

where $\mathcal{M}_{\text{TOT}}(Z)$ is the total simulated initial stellar mass, and $dN(z', z, Z)/dt(z)$ is the rate of BBHs forming from stars with initial metallicity Z at redshift z' and merging at z , extracted from our MOBSE catalogues. In COSMORATE, SFRD(z, Z) is given by

$$\text{SFRD}(z', Z) = \psi(z') p(z', Z), \quad (9)$$

where $\psi(z')$ is the cosmic SFR density at formation redshift z' , and $p(z', Z)$ is the log-normal distribution of metallicities Z at fixed formation redshift z' , with average $\mu(z')$ and spread σ_Z . Here, we take both $\psi(z)$ and $\mu(z)$ from Madau & Fragos (2017). Finally, we assume a metallicity spread $\sigma_Z = 0.3$.

2.7 Hyper-parametric model description

For each of our models (Table 3), described by their hyper-parameters λ , we predict the distributions of BBH mergers

$$\frac{dN}{d\theta}(\lambda) = N_{\lambda} p(\theta|\lambda), \quad (10)$$

where θ are the merger parameters, and N_{λ} is the total number of mergers predicted by the model. Assuming an instrumental horizon redshift $z_{\text{max}} = 1.5$, N_{λ} can be calculated as

$$N_{\lambda} = \int_0^{z_{\text{max}}} \mathcal{R}(z) \frac{dV_c}{dz} \frac{T_{\text{obs}}}{(1+z)} dz, \quad (11)$$

where $\frac{dV_c}{dz}$ is the comoving volume and T_{obs} the observation duration.

To model the population of merging BBHs, we have chosen five observable parameters $\theta = \{\mathcal{M}_c, q, z, \chi_{\text{eff}}, \chi_p\}$, where $\mathcal{M}_c = (m_1 m_2)^{3/5} / (m_1 + m_2)^{1/5}$ is the chirp mass in the source frame with m_1 (m_2) the masses of the primary (secondary) BH of the binary,

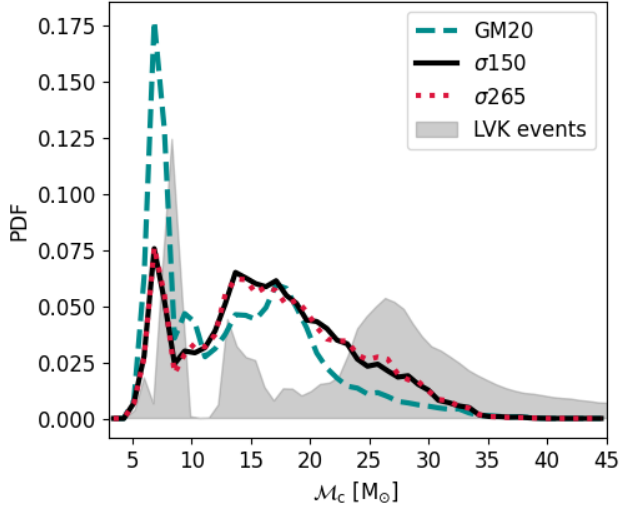


Figure 2. Predicted detectable distribution of chirp mass, for each kick model: GM20 (solid dark-cyan line), $\sigma150$ (dotted black line) and $\sigma265$ (dashed red line). For detectable distribution we mean the distribution of simulated BBHs with sufficiently high signal-to-noise ratio (Section 3). The shaded gray area is the distribution we obtain by stacking the posterior samples of the 59 confident detections from GWTC-3 (Appendix A).

$q = m_2/m_1$, and z is the redshift of the merger. In addition, we used two spin parameters: the effective spin (χ_{eff}) and the precessing spin (χ_p). The effective spin χ_{eff} is the mass-weighted projection of the two individual BH spins on the binary orbital angular momentum \vec{L}

$$\chi_{\text{eff}} = \frac{(\vec{\chi}_1 + q \vec{\chi}_2)}{1 + q} \cdot \frac{\vec{L}}{L}, \quad (12)$$

where $\vec{\chi}_{1,2} = \vec{s}_{1,2} c / (G m_{1,2}^2)$ is the dimensionless spin parameter of the two BHs. The precessing spin χ_p is defined as

$$\chi_p = \max(\chi_{1,\perp}, A \chi_{2,\perp}), \quad (13)$$

where $\chi_{1,\perp}$ ($\chi_{2,\perp}$) is the spin component of the primary (secondary) BH perpendicular to the orbital angular momentum vector \vec{L} , and $A = (4q + 3) / (4 + 3q)$.

To compute the distributions $p(\theta|\lambda)$, we constructed a catalogue of 10^6 sources for all possible combinations of hyper-parameters λ , using the merger rate density and the metallicity given by CosmoRAte. From these catalogues we derived continuous estimations of $p(\theta|\lambda)$ by making use of a Gaussian kernel density estimation assuming a bandwidth of 0.15.

3 HIERARCHICAL BAYESIAN INFERENCE

Given a set $\mathcal{H} = \{h^k\}_{k=1}^{N_{\text{obs}}}$ of N_{obs} GW observations, the posterior distribution of a set of hyper-parameters λ associated to an astrophysical model can be described as an in-homogeneous Poisson distribution (e.g., Loredano 2004; Mandel et al. 2019; Thrane & Talbot 2019; Bouffanais et al. 2019, 2021a,b):

$$p(\lambda, N_\lambda | \mathcal{H}) = e^{-\mu_\lambda} \pi(\lambda, N_\lambda) \prod_{k=1}^{N_{\text{obs}}} N_\lambda \int \mathcal{L}^k(h^k | \theta) p(\theta | \lambda) d\theta, \quad (14)$$

where N_{obs} is the number of events observed by the LVK, with an ensemble of parameters θ , N_λ is the number of predicted mergers

by the model (as calculated in eq. 11), μ_λ the number of predicted observations given a model and a detector, $\pi(\lambda, N_\lambda)$ are the prior distributions on λ and N_λ , and $\mathcal{L}^k(\{h^k\}^k | \theta)$ is the likelihood of the k^{th} observation.

The predicted number of events μ_λ can be written in terms of detection efficiency $\beta(\lambda)$ for a given model:

$$\mu_\lambda = N_\lambda \beta(\lambda), \quad \text{with} \quad \beta(\lambda) = \int_\theta p(\theta | \lambda) p_{\text{det}}(\theta) d\theta, \quad (15)$$

where $p_{\text{det}}(\theta)$ is the detection probability for a set of parameters θ . This probability can be inferred by computing the optimal signal to noise ratio (SNR) of the sources and comparing it to a detection threshold. In our case we chose as reference a threshold $\rho_{\text{thr}} = 8$ in the LIGO Livingston detector, for which we approximated the sensitivity using the measurements for the three runs separately (Abadie et al. 2010; Abbott et al. 2016b; Wysocki et al. 2018). The values for the event's log-likelihood were derived from the posterior and prior samples released by the LVK. Hence, the integral in eq. 14 is approximated with a Monte Carlo approach as

$$\mathcal{I}^k = \int \mathcal{L}^k(h^k | \theta) p(\theta | \lambda) d\theta \approx \frac{1}{N_s^k} \sum_{i=1}^{N_s^k} \frac{p(\theta_i^k | \lambda)}{\pi^k(\theta_i^k)}, \quad (16)$$

where θ_i^k is the i^{th} posterior sample of the k^{th} detection and N_s^k is the total number of posterior samples for the k^{th} detection. To compute the prior term in the denominator, we also used Gaussian kernel density estimation.

Finally, we can also choose to neglect the information coming from the number of sources predicted by the model when estimating the posterior distribution. By doing so, we can have some insights on the impact of the rate on the analysis. In practice, this can be done by marginalising eq. 14 over N_λ using a prior $\pi(N_\lambda) \sim 1/N_\lambda$ (Fishbach et al. 2018), which yields to the following expression for a model log-likelihood

$$\mathcal{L} = p(\lambda | \{h^k\}) \sim \pi(\lambda) \prod_{k=1}^{N_{\text{obs}}} \left[\frac{\mathcal{I}^k}{\beta(\lambda)} \right]. \quad (17)$$

We adopted the formalism described in eqs. 14–17 to perform a hierarchical Bayesian inference to compare the astrophysical models presented Sec. 2 with the third gravitational-wave transient catalogue (GWTC-3), the most updated catalogue of gravitational-wave events from the LVK (Abbott et al. 2021b,c). GWTC-3 contains 90 event candidates with probability of astrophysical origin $p_{\text{astro}} > 0.5$. From GWTC-3, we extract 59 confident detections of BBHs with a false alarm rate $\text{FAR} < 0.25 \text{ yr}^{-1}$. In this sub-sample, we do not include binary neutron stars and neutron star – BH systems, and we also exclude the other BBH candidates with an higher FAR. Our chosen FAR threshold ensures a sufficiently pure sample for our analysis (Abbott et al. 2021c). A list of the events used in this study is available in Appendix A. For the observable parameters θ , we use the choice described in Section 2.7, namely $\theta = \{\mathcal{M}_c, q, z, \chi_{\text{eff}}, \chi_p\}$.

4 RESULTS

4.1 Chirp mass

The chirp mass distribution (Fig. 2) does not depend on the spin model, by construction. Therefore, we only show different natal kicks. Models $\sigma150$ and $\sigma265$ show a similar distribution of chirp masses with two peaks of similar importance, one at $\mathcal{M}_c \approx 8 M_\odot$ and the

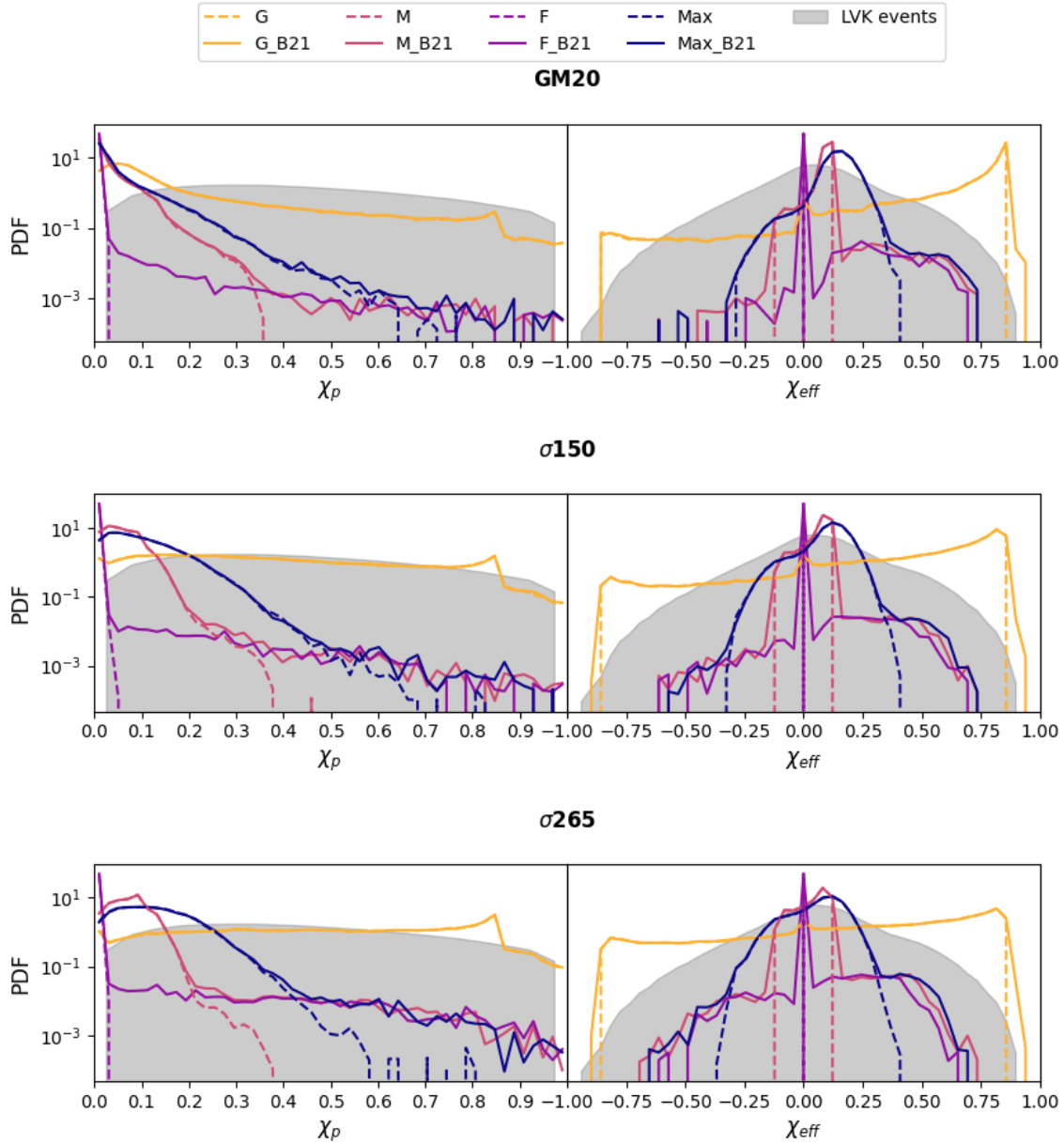


Figure 3. Predicted detectable distribution of χ_p (left) and χ_{eff} (right) for all of our models. Different colours refer to the spin model: G, M, F and Max. Solid (dashed) lines include (do not include) the tidal spin-up model by B21. From top to bottom: GM20, $\sigma 150$, and $\sigma 265$. The shaded gray areas are the distributions we obtain by stacking the posterior samples of the 59 confident detections from GWTC-3 (Appendix A).

other (broader) peak at $\mathcal{M}_c \approx 15 M_\odot$. In contrast, model GM20 has a much stronger preference for low-mass BHs, with a dominant peak at $\mathcal{M}_c \approx 8 M_\odot$. The reason for this difference is that all BHs in tight binary systems receive slow natal kicks in model GM20 (Fig. 1). This happens because stars in tight binary systems lose their envelope during mass transfer episodes; hence, the mass of supernova ejecta (m_{ej}) is small, triggering low kicks in model GM20.

Figure 2 also compares the detectable distribution of our models with the stacked posterior samples from the confident BBH detections in GWTC-3. This figure highlights two main differences between the population synthesis models and the posterior samples: the peak

at $\mathcal{M}_c \approx 15 M_\odot$ is stronger in the models than it is in the data, while the data present a more significant excess at $\mathcal{M}_c \approx 25 - 30 M_\odot$ than the models. Finally, the peak at $\mathcal{M}_c \approx 9 M_\odot$ in the data approximately matches the peak at $\mathcal{M}_c \approx 8 M_\odot$ in the models. The main features of our population synthesis models (in particular, the peaks at $\mathcal{M}_c \approx 8 - 10 M_\odot$ and $\mathcal{M}_c \approx 15 - 20 M_\odot$) are also common to other population-synthesis models (e.g., [Belczynski et al. 2020](#); [van Son et al. 2022](#)) and mostly spring from the core-collapse SN prescriptions by [Fryer et al. \(2012\)](#). Alternative core-collapse SN models (e.g., [Mapelli et al. 2020](#); [Mandel et al. 2021](#); [Patton et al.](#)

2022; Olejak et al. 2022) produce different features and deserve further investigation (Iorio et al., in prep.).

4.2 Spin parameters

Figure 3 shows the detectable distribution of spin parameters χ_p and χ_{eff} for all of our models. By construction, large spins are much more common in models G and G_B21, while models F and F_B21 have a strong predominance of vanishingly small spins. Models M, M_B21, Max and Max_B21 are intermediate between the other two extreme models.

Including or not the correction by B21 has negligible impact on the distribution of χ_p and χ_{eff} for models G, because of the predominance of large spin magnitudes. In contrast, introducing the spin-up correction by B21 has a key impact on models F, because it is the only way to account for mild to large spins in these models. The correction by B21 is important also for models M and Max, being responsible for the large-spin wings.

Finally, our model with slow kicks (GM20) results in a distribution of χ_p that is more peaked at zero (for models G, M and Max) with respect to the other two kick models ($\sigma 150$ and $\sigma 265$). In fact, the supernova kicks in model GM20 are not large enough to appreciably misalign BH spins (see Fig. 1).

A similar effect is visible in the distribution of χ_{eff} : model $\sigma 265$ produces a distribution of χ_{eff} that is less asymmetric about the zero with respect to models $\sigma 150$ and especially GM20.

4.3 Model Selection

Figure 4 and Table 4 report the values of the log-likelihood $\log \mathcal{L}$ defined in Eq. 17. We can quantify the difference between two models A and B by computing the average absolute difference in percentage

$$\Delta \log \mathcal{L}(A, B) = \left\langle \frac{2 |\log \mathcal{L}_i^A - \log \mathcal{L}_i^B|}{\log \mathcal{L}_i^A + \log \mathcal{L}_i^B} \right\rangle_{var}, \quad (18)$$

on the non-A,B variation var (var would be $\text{kick}(\text{spin})$ if A and B are spin(kick) models). For example to compare the two models G and G_B21, A and B become G_B21 and G and $var = \{\text{GM20}, \sigma 150, \sigma 265\}$.

The tidal spin-up mechanism (B21) affects the spin of a small part of the population of each model (Fig. 3). However, it improves the likelihood of the F and M models significantly (e.g., $\Delta \log \mathcal{L}(\text{M_B21}, \text{M}) = 89\%$, Table 4). This improvement of the log-likelihood can be explained by the presence of higher values of χ_p and χ_{eff} in the distribution of populations M_B21 and F_B21 compared to M and F (Fig. 3).

The F model yields $\mathcal{L}(\text{F}) = -\infty$ if we do not include the tidal spin-up correction, regardless of the kick model. This indicates that the LVK data do not support vanishingly small BH spins for the entire BBH population. However, it is sufficient to inject a tiny sub-population of spinning BHs, by switching on the B21 correction, and the F model becomes one of the best considered models. In fact, the F_B21 models only includes 0.4% of BHs with $\chi > 0.01$ and achieves $\log \mathcal{L} > 200$ (for spin models $\sigma 150$ and $\sigma 265$).

The G and G_B21 spin models exhibit lower log-likelihood values than the others for all kicks models: $\log \mathcal{L} \leq 150$ for $\sigma 150$ and $\sigma 265$, and $\log \mathcal{L} < 0$ for GM20. This happens because the distribution of χ_{eff} has non-negligible support for extreme values $\chi_{\text{eff}} < -0.5$ and $\chi_{\text{eff}} > 0.5$ (Fig. 3).

The kick models $\sigma 150$ and $\sigma 265$ show similar results ($\Delta \log \mathcal{L}(\sigma 150, \sigma 265) < 3\%$) for every spin assumptions. Also,

Table 4. Log-likelihood \mathcal{L} (Eq. 17) estimated with five merger parameters $\theta = \{\mathcal{M}_c, z, \chi_{\text{eff}}, q, \chi_p\}$.

Model Name	GM20	$\sigma 150$	$\sigma 265$
G	-1	149	145
G_B21	-12	150	141
M	0	162	171
M_B21	36	232	232
F	$-\infty$	$-\infty$	$-\infty$
F_B21	88	250	242
Max	92	255	254
Max_B21	106	257	250

Table 5. Log-likelihood \mathcal{L} (Eq. 17) estimated with four merger parameters $\theta = \{\mathcal{M}_c, z, \chi_{\text{eff}}, q\}$. Here, we ignore χ_p .

Model Name	GM20	$\sigma 150$	$\sigma 265$
G	35	146	147
G_B21	47	149	154
M	141	192	190
M_B21	130	199	180
F	85	146	138
F_B21	185	207	180
Max	161	208	155
Max_B21	160	206	200

for all spin assumptions, the GM20 kick model scores a significantly lower likelihood than the other models $\sigma 150$ and $\sigma 265$ with $\Delta \log \mathcal{L}(\sigma 150, \text{GM20}) \sim \Delta \log \mathcal{L}(\sigma 265, \text{GM20}) \sim 150\%$. This result can be explained by the high peak of model GM20 at low chirp masses ($\mathcal{M}_c \sim 8M_\odot$, see Sec.4.1 and Fig.2) and by the low value of χ_p compared to the other kick models (Fig. 3).

Models Max and Max_B21 are possibly the best match to the data, but this is not surprising, because they were built as a toy model to visually match the data. Among the astrophysically-motivated models (i.e., after excluding the Max model), M, M_B21 and F_B21 (with kick models $\sigma 150$ and $\sigma 265$) are the most favoured by the data. This might be interpreted as a support for the Tayler-Spruit instability mechanism (adopted in models M) and for the tidal spin-up model by B21.

4.4 Importance of χ_p

The χ_p parameter encodes information on the spin component in the orbital plane. Its impact on gravitational-wave signals is much lower than that of χ_{eff} , and therefore its measurement is less precise. To understand the impact of χ_p on our results, we re-ran the analysis without this parameter. The results are shown in Table 5 and in Fig. 4 with empty markers. Fig. 4 shows that, if we do not include χ_p , the models M and M_B21 have almost the same log-likelihood, and even the F model yields a positive log-likelihood. Furthermore, the analysis without χ_p results in significantly larger values of \mathcal{L} for the kick model GM20. Our results demonstrate that the measured χ_p of GWTC-3 BBHs carries substantial information, despite the large uncertainties.

5 DISCUSSION

The spin magnitude of BHs is largely uncertain, mostly because we do not fully understand angular momentum transport in massive stars. Here, we have taken a number of spin models bracketing the

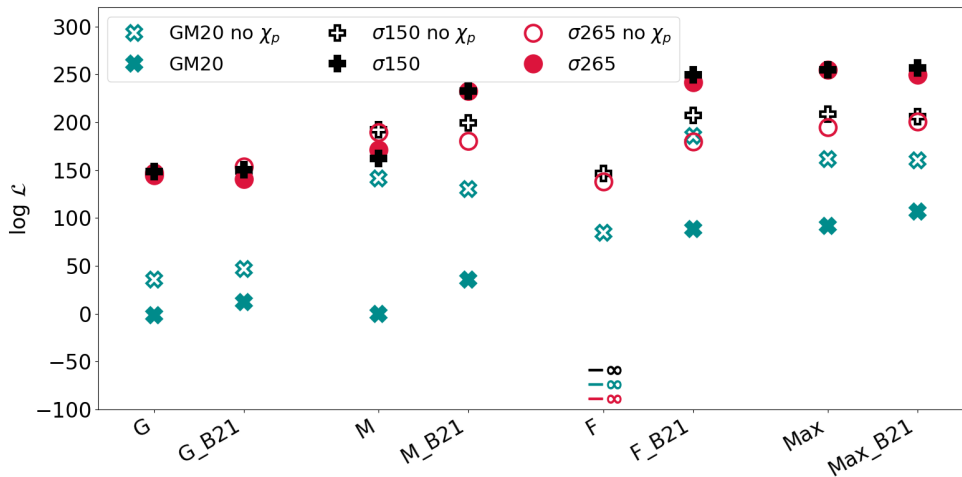


Figure 4. Values of the log-likelihood \mathcal{L} defined in Eq. 17 for the four different models Geneva (G), MESA (M), Fuller (F), and Maxwellian (Max), with/without the tidal spin-up mechanism (B21). Blue crosses: GM20; dark pluses: $\sigma150$; red circles: $\sigma265$.

main uncertainties, we have implemented them into our population-synthesis code `MOBSE`, and compared them against GWTC-3 data within a hierarchical Bayesian framework.

The data do not support models in which the entire BH population has vanishingly small spins (model F). This result is mainly driven by the χ_p parameter. This is in agreement with, e.g., the complementary analysis presented in Callister et al. (2022). They employed a variety of complementary methods to measure the distribution of spin magnitudes and orientations of BBH mergers, and concluded that the existence of a sub-population of BHs with vanishing spins is not required by current data. Callister et al. (2022) find that the fraction of non-spinning BHs can comprise up to $\sim 60 - 70\%$ of the total population. In our F_B21 models, we have $\sim 99.6\%$ of BHs with $\chi < 0.01$.

Recently, Biscoveanu et al. (2021); Roulet et al. (2021); Galaudage et al. (2021) and Tong et al. (2022) claimed the existence of a sub-population of zero-spin BHs. From our analysis, we cannot exclude the existence of such sub-population, as the F model with B21 correction (F_B21) still represents a good match of the data. Similarly to Belczynski et al. (2020) and Gerosa et al. (2018), we find that models with large spins (G, G_B21) are less favoured by the data, but they are still acceptable if we allow for large kicks.

Overall, we find a preference for large natal kicks. This result goes into the same direction as the work by Callister et al. (2021). Actually, this preference for large natal kicks is degenerate with the adopted formation channel. Had we included the dynamical formation channel in dense star clusters, we would have added a sub-population of isotropically oriented spins (see, e.g., Figure 8 of Mapelli et al. 2022). In a forthcoming study, we will extend our analysis to a multi-channel analysis. While it is unlikely that BBH mergers only originate from one single channel, adding more formation channels to a hierarchical Bayesian analysis dramatically increases the number of parameters, making it more difficult to reject some portions of the parameter space.

6 SUMMARY

The origin of BH spins is still controversial, and angular momentum transport inside massive stars is one of the main sources of uncertainty. Here, we apply hierarchical Bayesian inference to derive

constraints on spin models from the 59 most confident BBH merger events in GWTC-3. We consider five parameters: chirp mass, mass ratio, redshift, effective spin, and precessing spin.

For model selection, we use a set of binary population synthesis simulations spanning different assumptions for black hole spins and natal kicks. In particular, our spin models account for relatively inefficient (G), efficient (Max and M), and very efficient angular-momentum transport (F). A higher efficiency of angular momentum transport is associated with lower BH spins. In particular, model F predicts vanishingly small spins for the entire BH population. For each of our models, we also include the possibility that some BHs are tidally spun-up (B21). We considered three different natal kick models: according to models $\sigma265$ and $\sigma150$, we randomly draw the kicks from a Maxwellian curve with $\sigma = 265$ and 150 km s^{-1} , respectively; in the third model (G20), we also derive the kicks from a Maxwellian curve with $\sigma = 265 \text{ km s}^{-1}$, but the kick magnitude is then modulated by the ratio between the mass of the ejecta and the mass of the BH.

We summarize our main results as follows.

- The data from GWTC-3 do not support models in which the entire BH population has vanishingly small spins (model F).
- In contrast, models in which most spins are vanishingly small, but that also include a sub-population of tidally spun-up BHs (model F_B21) are a good match to the data.
- The models in which angular momentum transport is relatively inefficient (G and G_21) yield log-likelihood values that are much lower than models with efficient angular momentum transport (M, M_B21, Max, and Max_B21).
- Models with large BH kicks ($\sigma150$ and $\sigma265$) are favoured by our analysis with respect to low-kick models (G20).
- Our results show that the precessing spin parameter χ_p plays a crucial impact to constrain the spin distribution of BBH mergers.

ACKNOWLEDGEMENTS

MM, CP, FS and YB acknowledge financial support from the European Research Council for the ERC Consolidator grant DE-MOBLACK, under contract no. 770017. This research has made use of data or software obtained from the Gravitational Wave Open

Science Center (gwosc.org), a service of LIGO Laboratory, the LIGO Scientific Collaboration, the Virgo Collaboration, and KAGRA. LIGO Laboratory and Advanced LIGO are funded by the United States National Science Foundation (NSF) as well as the Science and Technology Facilities Council (STFC) of the United Kingdom, the Max-Planck-Society (MPS), and the State of Niedersachsen/Germany for support of the construction of Advanced LIGO and construction and operation of the GEO600 detector. Additional support for Advanced LIGO was provided by the Australian Research Council. Virgo is funded, through the European Gravitational Observatory (EGO), by the French Centre National de Recherche Scientifique (CNRS), the Italian Istituto Nazionale di Fisica Nucleare (INFN) and the Dutch Nikhef, with contributions by institutions from Belgium, Germany, Greece, Hungary, Ireland, Japan, Monaco, Poland, Portugal, Spain. KAGRA is supported by Ministry of Education, Culture, Sports, Science and Technology (MEXT), Japan Society for the Promotion of Science (JSPS) in Japan; National Research Foundation (NRF) and Ministry of Science and ICT (MSIT) in Korea; Academia Sinica (AS) and National Science and Technology Council (NSTC) in Taiwan [Abbott et al. \(2021e\)](#); [The LIGO Scientific Collaboration et al. \(2023\)](#). This research made use of NUMPY ([Harris et al. 2020](#)), and SCIPY ([Virtanen et al. 2020](#)). For the plots we used MATPLOTLIB ([Hunter 2007](#)).

DATA AVAILABILITY

The data underlying this article will be shared on reasonable request to the corresponding author. The latest public version of MOBSE can be downloaded from [this repository](#). COSMORATE can be downloaded from [this link](#).

REFERENCES

- Aasi J., et al., 2015, *Classical and Quantum Gravity*, **32**, 074001
- Abadie J., et al., 2010, *Classical and Quantum Gravity*, **27**, 173001
- Abbott B. P., et al., 2016a, *Phys. Rev. Lett.*, **116**, 241103
- Abbott B. P., et al., 2016b, *ApJ*, **833**, L1
- Abbott B. P., et al., 2019, *Physical Review X*, **9**, 031040
- Abbott R., et al., 2020, *Phys. Rev. D*, **102**, 043015
- Abbott R., et al., 2021a, arXiv e-prints, p. [arXiv:2108.01045](#)
- Abbott R., et al., 2021b, arXiv e-prints, p. [arXiv:2111.03606](#)
- Abbott R., et al., 2021c, arXiv e-prints, p. [arXiv:2111.03634](#)
- Abbott R., et al., 2021d, *Physical Review X*, **11**, 021053
- Abbott R., et al., 2021e, *SoftwareX*, **13**, 100658
- Acernese F., et al., 2015, *Classical and Quantum Gravity*, **32**, 024001
- Aerts C., Mathis S., Rogers T. M., 2019, *ARA&A*, **57**, 35
- Aghanim N., et al., 2020, *A&A*, **641**, A6
- Arca Sedda M., Benacquista M., 2019, *MNRAS*, **482**, 2991
- Arca Sedda M., Mapelli M., Spera M., Benacquista M., Giacobbo N., 2020, *ApJ*, **894**, 133
- Atri P., et al., 2019, *MNRAS*, **489**, 3116
- Baibhav V., Gerosa D., Berti E., Wong K. W. K., Helfer T., Mould M., 2020, *Phys. Rev. D*, **102**, 043002
- Barrett J. W., Gaebel S. M., Neijssel C. J., Vigna-Gómez A., Stevenson S., Berry C. P. L., Farr W. M., Mandel I., 2018, *MNRAS*, **477**, 4685
- Bavera S. S., et al., 2020, *A&A*, **635**, A97
- Bavera S. S., Zevin M., Fragos T., 2021, *Research Notes of the American Astronomical Society*, **5**, 127
- Belczynski K., Bulik T., Fryer C. L., Ruiter A., Valsecchi F., Vink J. S., Hurley J. R., 2010, *ApJ*, **714**, 1217
- Belczynski K., et al., 2020, *A&A*, **636**, A104
- Biscoveanu S., Isi M., Vitale S., Varma V., 2021, *Phys. Rev. Lett.*, **126**, 171103
- Bouffanais Y., Mapelli M., Gerosa D., Di Carlo U. N., Giacobbo N., Berti E., Baibhav V., 2019, *ApJ*, **886**, 25
- Bouffanais Y., Mapelli M., Santoliquido F., Giacobbo N., Iorio G., Costa G., 2021a, *MNRAS*, **505**, 3873
- Bouffanais Y., Mapelli M., Santoliquido F., Giacobbo N., Di Carlo U. N., Rastello S., Artale M. C., Iorio G., 2021b, *MNRAS*, **507**, 5224
- Briel M. M., Stevance H. F., Eldridge J. J., 2022, arXiv e-prints, p. [arXiv:2206.13842](#)
- Broekgaarden F. S., et al., 2022a, *MNRAS*, **516**, 5737
- Broekgaarden F. S., Stevenson S., Thrane E., 2022b, *ApJ*, **938**, 45
- Callister T. A., Farr W. M., Renzo M., 2021, *ApJ*, **920**, 157
- Callister T. A., Miller S. J., Chatzizoannou K., Farr W. M., 2022, arXiv e-prints, p. [arXiv:2205.08574](#)
- Cantiello M., Mankovich C., Bildsten L., Christensen-Dalsgaard J., Paxton B., 2014, *ApJ*, **788**, 93
- Chattopadhyay D., Hurley J., Stevenson S., Raidani A., 2022, *MNRAS*, **513**, 4527
- Claeys J. S. W., Pols O. R., Izzard R. G., Vink J., Verbunt F. W. M., 2014, *A&A*, **563**, A83
- Costa G., Girardi L., Bressan A., Marigo P., Rodrigues T. S., Chen Y., Lanza A., Goudfrooij P., 2019, *MNRAS*, **485**, 4641
- Dall’Amico M., Mapelli M., Di Carlo U. N., Bouffanais Y., Rastello S., Santoliquido F., Ballone A., Arca Sedda M., 2021, *MNRAS*, **508**, 3045
- Di Carlo U. N., Giacobbo N., Mapelli M., Pasquato M., Spera M., Wang L., Haardt F., 2019, *MNRAS*, **487**, 2947
- Ekström S., et al., 2012, *A&A*, **537**, A146
- Eldridge J. J., Stanway E. R., 2016, *MNRAS*, **462**, 3302
- Farr W. M., Sravan N., Cantrell A., Kreidberg L., Bailyn C. D., Mandel I., Kalogera V., 2011, *ApJ*, **741**, 103
- Farr W. M., Stevenson S., Miller M. C., Mandel I., Farr B., Vecchio A., 2017, *Nature*, **548**, 426
- Farr B., Holz D. E., Farr W. M., 2018, *ApJ*, **854**, L9
- Fishbach M., Holz D. E., 2017, *ApJ*, **851**, L25
- Fishbach M., Kalogera V., 2022, *ApJ*, **929**, L26
- Fishbach M., Holz D. E., Farr W. M., 2018, *The Astrophysical Journal*, **863**, L41
- Fragione G., Kocsis B., 2020, *Mon. Not. Roy. Astron. Soc.*, **493**, 3920
- Fragione G., Kocsis B., Rasio F. A., Silk J., 2022, *Astrophys. J.*, **927**, 231
- Fragos T., McClintock J. E., 2015, *ApJ*, **800**, 17
- Fryer C. L., Kalogera V., 2001, *ApJ*, **554**, 548
- Fryer C. L., Belczynski K., Wiktorowicz G., Dominik M., Kalogera V., Holz D. E., 2012, *ApJ*, **749**, 91
- Fryer C. L., Olejak A., Belczynski K., 2022, *ApJ*, **931**, 94
- Fuller J., Ma L., 2019, *ApJ*, **881**, L1
- Fuller J., Piro A. L., Jermyn A. S., 2019, *MNRAS*, **485**, 3661
- Galaudage S., Talbot C., Nagar T., Jain D., Thrane E., Mandel I., 2021, *ApJ*, **921**, L15
- Gehan C., Mosser B., Michel E., Samadi R., Kallinger T., 2018, *A&A*, **616**, A24
- Gerosa D., Kesden M., Berti E., O’Shaughnessy R., Sperhake U., 2013, *Phys. Rev. D*, **87**, 104028
- Gerosa D., Berti E., O’Shaughnessy R., Belczynski K., Kesden M., Wysocki D., Gladysz W., 2018, *Phys. Rev. D*, **98**, 084036
- Giacobbo N., Mapelli M., 2018, *MNRAS*, **480**, 2011
- Giacobbo N., Mapelli M., 2019, *MNRAS*, **482**, 2234
- Giacobbo N., Mapelli M., 2020, *ApJ*, **891**, 141
- Giacobbo N., Mapelli M., Spera M., 2018, *MNRAS*, **474**, 2959
- Hannam M., et al., 2022, *Nature*, **610**, 652
- Harris C. R., et al., 2020, *Nature*, **585**, 357
- Heger A., Fryer C. L., Woosley S. E., Langer N., Hartmann D. H., 2003, *ApJ*, **591**, 288
- Hobbs G., Lorimer D. R., Lyne A. G., Kramer M., 2005, *MNRAS*, **360**, 974
- Hotokezaka K., Piran T., 2017, *ApJ*, **842**, 111
- Hunter J. D., 2007, *Computing in Science & Engineering*, **9**, 90
- Hurley J. R., Pols O. R., Tout C. A., 2000, *MNRAS*, **315**, 543
- Hurley J. R., Tout C. A., Pols O. R., 2002, *MNRAS*, **329**, 897
- Kalogera V., 2000, *ApJ*, **541**, 319

- Kimball C., Talbot C., Berry C. P. L., Carney M., Zevin M., Thrane E., Kalogera V., 2020, *ApJ*, **900**, 177
- Kimball C., et al., 2021, *Astrophys. J. Lett.*, 915, L35
- Kroupa P., 2001, *MNRAS*, **322**, 231
- Kushnir D., Zaldarriaga M., Kollmeier J. A., Waldman R., 2016, *MNRAS*, **462**, 844
- Limongi M., Chieffi A., 2018, *ApJS*, **237**, 13
- Loredò T. J., 2004, in Fischer R., Preuss R., Toussaint U. V., eds, American Institute of Physics Conference Series Vol. 735, Bayesian Inference and Maximum Entropy Methods in Science and Engineering: 24th International Workshop on Bayesian Inference and Maximum Entropy Methods in Science and Engineering. pp 195–206 (arXiv:astro-ph/0409387), doi:10.1063/1.1835214
- Maccarone T. J., Kundu A., Zepf S. E., Rhode K. L., 2007, *Nature*, **445**, 183
- Madau P., Fragos T., 2017, *ApJ*, **840**, 39
- Maeder A., Meynet G., 2000, *ARA&A*, **38**, 143
- Mandel I., Farr W. M., Gair J. R., 2019, *MNRAS*, **486**, 1086
- Mandel I., Müller B., Riley J., de Mink S. E., Vigna-Gómez A., Chattopadhyay D., 2021, *MNRAS*, **500**, 1380
- Mapelli M., Zampieri L., Ripamonti E., Bressan A., 2013, *MNRAS*, **429**, 2298
- Mapelli M., Giacobbo N., Ripamonti E., Spera M., 2017, *MNRAS*, **472**, 2422
- Mapelli M., Spera M., Montanari E., Limongi M., Chieffi A., Giacobbo N., Bressan A., Bouffanais Y., 2020, *ApJ*, **888**, 76
- Mapelli M., et al., 2021, *MNRAS*, **505**, 339
- Mapelli M., Bouffanais Y., Santoliquido F., Arca Sedda M., Artale M. C., 2022, *MNRAS*, **511**, 5797
- Marchant P., Langer N., Podsiadlowski P., Tauris T. M., Moriya T. J., 2016, *A&A*, **588**, A50
- Miller-Jones J. C. A., et al., 2021, *Science*, **371**, 1046
- Miller S., Callister T. A., Farr W. M., 2020, *ApJ*, **895**, 128
- Mosser B., et al., 2012, *A&A*, **548**, A10
- Motta S. E., Belloni T. M., Stella L., Muñoz-Darias T., Fender R., 2014, *MNRAS*, **437**, 2554
- Olejak A., Belczynski K., 2021, *ApJ*, **921**, L2
- Olejak A., Fryer C. L., Belczynski K., Baibhav V., 2022, *MNRAS*, **516**, 2252
- Olsen S., Venumadhav T., Mushkin J., Roulet J., Zackay B., Zaldarriaga M., 2022, *Phys. Rev. D*, **106**, 043009
- Özel F., Psaltis D., Narayan R., McClintock J. E., 2010, *ApJ*, **725**, 1918
- Patton R. A., Sukhbold T., Eldridge J. J., 2022, *MNRAS*, **511**, 903
- Perna R., Artale M. C., Wang Y.-H., Mapelli M., Lazzati D., Sgalletta C., Santoliquido F., 2022, *MNRAS*, **512**, 2654
- Qin Y., Fragos T., Meynet G., Andrews J., Sørensen M., Song H. F., 2018, *A&A*, **616**, A28
- Qin Y., Fragos T., Meynet G., Marchant P., Kalogera V., Andrews J., Sørensen M., Song H. F., 2019, *IAU Symposium*, **346**, 426
- Repetto S., Igoshev A. P., Nelemans G., 2017, *MNRAS*, **467**, 298
- Reynolds C. S., 2021, *ARA&A*, **59**, 117
- Rodríguez C. L., Zevin M., Pankow C., Kalogera V., Rasio F. A., 2016, *ApJ*, **832**, L2
- Roulet J., Zaldarriaga M., 2019, *MNRAS*, **484**, 4216
- Roulet J., Chia H. S., Olsen S., Dai L., Venumadhav T., Zackay B., Zaldarriaga M., 2021, *Phys. Rev. D*, **104**, 083010
- Sana H., et al., 2012, *Science*, **337**, 444
- Santoliquido F., Mapelli M., Bouffanais Y., Giacobbo N., Di Carlo U. N., Rastello S., Artale M. C., Ballone A., 2020, *ApJ*, **898**, 152
- Santoliquido F., Mapelli M., Giacobbo N., Bouffanais Y., Artale M. C., 2021, *MNRAS*, **502**, 4877
- Shafee R., McClintock J. E., Narayan R., Davis S. W., Li L.-X., Remillard R. A., 2006, *ApJ*, **636**, L113
- Spera M., Mapelli M., 2017, *MNRAS*, **470**, 4739
- Spruit H. C., 2002, *A&A*, **381**, 923
- Stegmann J., Antonini F., 2021, *Phys. Rev. D*, **103**, 063007
- Stevenson S., 2022, *ApJ*, **926**, L32
- Stevenson S., Clarke T. A., 2022, *MNRAS*,
- Stevenson S., Ohme F., Fairhurst S., 2015, *ApJ*, **810**, 58
- Stevenson S., Berry C. P. L., Mandel I., 2017, *MNRAS*, **471**, 2801
- Talbot C., Thrane E., 2017, *Phys. Rev. D*, **96**, 023012
- Tauris T. M., Langer N., Podsiadlowski P., 2015, *MNRAS*, **451**, 2123
- Tauris T. M., et al., 2017, *ApJ*, **846**, 170
- Taylor S. R., Gerosa D., 2018, *Phys. Rev. D*, **98**, 083017
- The LIGO Scientific Collaboration et al., 2023, *arXiv e-prints*, p. arXiv:2302.03676
- Thrane E., Talbot C., 2019, *Publ. Astron. Soc. Australia*, **36**, e010
- Tiwari V., Fairhurst S., Hannam M., 2018, *ApJ*, **868**, 140
- Tong H., Galadage S., Thrane E., 2022, *Phys. Rev. D*, **106**, 103019
- Venumadhav T., Zackay B., Roulet J., Dai L., Zaldarriaga M., 2020, *Phys. Rev. D*, **101**, 083030
- Vink J. S., de Koter A., Lamers H. J. G. L. M., 2001, *A&A*, **369**, 574
- Virtanen P., et al., 2020, *Nature Methods*, **17**, 261
- Vitale S., Lynch R., Sturani R., Graff P., 2017, *Classical and Quantum Gravity*, **34**, 03LT01
- Wysocki D., Gerosa D., O’Shaughnessy R., Belczynski K., Gladysz W., Berti E., Kesden M., Holz D. E., 2018, *Phys. Rev. D*, **97**, 043014
- Wysocki D., Lange J., O’Shaughnessy R., 2019, *Phys. Rev. D*, **100**, 043012
- Zahn J. P., 1992, *A&A*, **265**, 115
- Zaldarriaga M., Kushnir D., Kollmeier J. A., 2018, *MNRAS*, **473**, 4174
- Zevin M., Pankow C., Rodríguez C. L., Sampson L., Chase E., Kalogera V., Rasio F. A., 2017, *ApJ*, **846**, 82
- Zevin M., et al., 2021, *ApJ*, **910**, 152
- de Mink S. E., Mandel I., 2016, *MNRAS*, **460**, 3545
- van Son L. A. C., et al., 2022, *Astrophys. J.*, **940**, 184

APPENDIX A: SAMPLE OF GRAVITATIONAL-WAVE EVENTS

Table A1 lists all the gravitational-wave event candidates we used in our study. From GWTC-3, we selected all the event candidates with $p_{\text{astro}} > 0.9$ and $\text{FAR} < 0.25 \text{ yr}^{-1}$, excluding the following three systems:

- the binary neutron star GW170807;
- the (possible) neutron star–BH binary system GW190814;
- the BBH GW190521 ($m_1 = 98.4^{+33.6}_{-21.7} M_{\odot}$, $m_2 = 57.2^{+27.1}_{-30.1} M_{\odot}$ Abbott et al. 2021b), which can form only via dynamical interactions in our models (e.g., Di Carlo et al. 2019; Dall’Amico et al. 2021; Mapelli et al. 2021).

This paper has been typeset from a \LaTeX file prepared by the author.

Table A1. Catalogue of BBH events adopted in this study. the uncertainties shown stand for the 90% credible intervals.

Name	$M_c [M_\odot]$	q	χ_{eff}	χ_p	z
GW150914	$28.6^{+1.7}_{-1.5}$	$0.86^{+0.12}_{-0.2}$	$-0.01^{+0.12}_{-0.13}$	$0.34^{+0.45}_{-0.25}$	$0.09^{+0.03}_{-0.03}$
GW151012	$15.2^{+2.1}_{-1.2}$	$0.59^{+0.36}_{-0.35}$	$0.05^{+0.31}_{-0.2}$	$0.33^{+0.45}_{-0.25}$	$0.21^{+0.09}_{-0.09}$
GW151226	$8.9^{+0.3}_{-0.3}$	$0.56^{+0.38}_{-0.33}$	$0.18^{+0.2}_{-0.12}$	$0.49^{+0.39}_{-0.32}$	$0.09^{+0.04}_{-0.04}$
GW170104	$21.4^{+2.2}_{-1.8}$	$0.65^{+0.3}_{-0.23}$	$-0.04^{+0.17}_{-0.21}$	$0.36^{+0.42}_{-0.27}$	$0.2^{+0.08}_{-0.08}$
GW170608	$7.9^{+0.2}_{-0.2}$	$0.69^{+0.28}_{-0.36}$	$0.03^{+0.19}_{-0.07}$	$0.36^{+0.45}_{-0.27}$	$0.07^{+0.02}_{-0.02}$
GW170729	$35.4^{+6.5}_{-4.8}$	$0.68^{+0.28}_{-0.28}$	$0.37^{+0.21}_{-0.25}$	$0.44^{+0.35}_{-0.28}$	$0.49^{+0.19}_{-0.21}$
GW170809	$24.9^{+2.1}_{-1.7}$	$0.68^{+0.28}_{-0.24}$	$0.08^{+0.17}_{-0.17}$	$0.35^{+0.43}_{-0.26}$	$0.2^{+0.05}_{-0.07}$
GW170814	$24.1^{+1.4}_{-1.1}$	$0.83^{+0.15}_{-0.23}$	$0.07^{+0.12}_{-0.12}$	$0.48^{+0.41}_{-0.36}$	$0.12^{+0.03}_{-0.04}$
GW170818	$26.5^{+2.1}_{-1.7}$	$0.76^{+0.21}_{-0.25}$	$-0.09^{+0.18}_{-0.21}$	$0.49^{+0.37}_{-0.34}$	$0.21^{+0.07}_{-0.07}$
GW170823	$29.2^{+4.6}_{-3.6}$	$0.74^{+0.23}_{-0.3}$	$0.09^{+0.22}_{-0.26}$	$0.42^{+0.41}_{-0.31}$	$0.35^{+0.15}_{-0.15}$
GW190408_181802	$18.3^{+1.9}_{-1.2}$	$0.75^{+0.21}_{-0.24}$	$-0.03^{+0.14}_{-0.19}$	$0.39^{+0.37}_{-0.31}$	$0.29^{+0.06}_{-0.1}$
GW190412	$13.3^{+0.4}_{-0.3}$	$0.28^{+0.12}_{-0.06}$	$0.25^{+0.08}_{-0.11}$	$0.3^{+0.19}_{-0.16}$	$0.15^{+0.03}_{-0.03}$
GW190413_052954	$24.6^{+5.5}_{-4.1}$	$0.69^{+0.27}_{-0.29}$	$-0.01^{+0.29}_{-0.34}$	$0.41^{+0.43}_{-0.31}$	$0.59^{+0.29}_{-0.24}$
GW190413_134308	$33.0^{+8.2}_{-5.4}$	$0.69^{+0.28}_{-0.31}$	$-0.03^{+0.25}_{-0.29}$	$0.56^{+0.37}_{-0.41}$	$0.71^{+0.31}_{-0.3}$
GW190421_213856	$31.2^{+5.9}_{-4.2}$	$0.79^{+0.19}_{-0.3}$	$-0.06^{+0.22}_{-0.27}$	$0.48^{+0.4}_{-0.36}$	$0.49^{+0.19}_{-0.21}$
GW190503_185404	$30.2^{+4.2}_{-4.2}$	$0.65^{+0.29}_{-0.23}$	$-0.03^{+0.2}_{-0.26}$	$0.38^{+0.42}_{-0.29}$	$0.27^{+0.11}_{-0.11}$
GW190512_180714	$14.6^{+1.3}_{-1.0}$	$0.54^{+0.37}_{-0.18}$	$0.03^{+0.12}_{-0.13}$	$0.22^{+0.37}_{-0.17}$	$0.27^{+0.09}_{-0.1}$
GW190513_205428	$21.6^{+3.8}_{-1.9}$	$0.5^{+0.42}_{-0.18}$	$0.11^{+0.28}_{-0.17}$	$0.31^{+0.39}_{-0.23}$	$0.37^{+0.13}_{-0.13}$
GW190517_055101	$26.6^{+4.0}_{-4.0}$	$0.68^{+0.27}_{-0.29}$	$0.52^{+0.19}_{-0.19}$	$0.49^{+0.3}_{-0.29}$	$0.34^{+0.24}_{-0.14}$
GW190519_153544	$44.5^{+6.4}_{-7.1}$	$0.61^{+0.28}_{-0.19}$	$0.31^{+0.2}_{-0.22}$	$0.44^{+0.35}_{-0.29}$	$0.44^{+0.25}_{-0.14}$
GW190521_074359	$32.1^{+3.2}_{-2.5}$	$0.78^{+0.19}_{-0.21}$	$0.09^{+0.13}_{-0.13}$	$0.4^{+0.32}_{-0.29}$	$0.24^{+0.07}_{-0.1}$
GW190602_175927	$49.1^{+9.1}_{-8.5}$	$0.71^{+0.25}_{-0.33}$	$0.07^{+0.25}_{-0.24}$	$0.42^{+0.41}_{-0.31}$	$0.47^{+0.25}_{-0.17}$
GW190620_030421	$38.3^{+8.3}_{-6.5}$	$0.62^{+0.32}_{-0.27}$	$0.33^{+0.22}_{-0.25}$	$0.43^{+0.36}_{-0.28}$	$0.49^{+0.23}_{-0.2}$
GW190630_185205	$24.9^{+2.1}_{-2.1}$	$0.68^{+0.27}_{-0.22}$	$0.1^{+0.12}_{-0.13}$	$0.32^{+0.31}_{-0.23}$	$0.18^{+0.1}_{-0.07}$
GW190701_203306	$40.3^{+5.4}_{-4.9}$	$0.76^{+0.21}_{-0.31}$	$-0.07^{+0.23}_{-0.29}$	$0.42^{+0.42}_{-0.31}$	$0.37^{+0.11}_{-0.12}$
GW190706_222641	$42.7^{+10.0}_{-7.0}$	$0.58^{+0.34}_{-0.25}$	$0.28^{+0.26}_{-0.29}$	$0.38^{+0.39}_{-0.28}$	$0.71^{+0.32}_{-0.27}$
GW190707_093326	$8.5^{+0.6}_{-0.5}$	$0.73^{+0.24}_{-0.27}$	$-0.05^{+0.1}_{-0.08}$	$0.29^{+0.39}_{-0.23}$	$0.16^{+0.07}_{-0.07}$
GW190708_232457	$13.2^{+0.9}_{-0.6}$	$0.76^{+0.21}_{-0.28}$	$0.02^{+0.1}_{-0.08}$	$0.29^{+0.43}_{-0.23}$	$0.18^{+0.06}_{-0.07}$
GW190720_000836	$8.9^{+0.5}_{-0.8}$	$0.58^{+0.36}_{-0.3}$	$0.18^{+0.14}_{-0.12}$	$0.33^{+0.43}_{-0.22}$	$0.16^{+0.12}_{-0.06}$
GW190727_060333	$28.6^{+5.3}_{-3.7}$	$0.8^{+0.18}_{-0.32}$	$0.11^{+0.26}_{-0.25}$	$0.47^{+0.41}_{-0.36}$	$0.55^{+0.21}_{-0.22}$
GW190728_064510	$8.6^{+0.5}_{-0.3}$	$0.66^{+0.3}_{-0.37}$	$0.12^{+0.2}_{-0.07}$	$0.29^{+0.37}_{-0.2}$	$0.18^{+0.05}_{-0.07}$
GW190803_022701	$27.3^{+5.7}_{-4.1}$	$0.75^{+0.22}_{-0.31}$	$-0.03^{+0.24}_{-0.27}$	$0.44^{+0.42}_{-0.33}$	$0.55^{+0.26}_{-0.24}$
GW190828_063405	$25.0^{+3.4}_{-2.1}$	$0.82^{+0.15}_{-0.22}$	$0.19^{+0.15}_{-0.16}$	$0.43^{+0.36}_{-0.3}$	$0.38^{+0.15}_{-0.15}$
GW190828_065509	$13.3^{+1.2}_{-1.0}$	$0.43^{+0.38}_{-0.16}$	$0.08^{+0.16}_{-0.16}$	$0.3^{+0.38}_{-0.23}$	$0.3^{+0.1}_{-0.1}$
GW190910_112807	$34.3^{+4.1}_{-4.1}$	$0.82^{+0.15}_{-0.23}$	$0.02^{+0.18}_{-0.18}$	$0.4^{+0.39}_{-0.32}$	$0.28^{+0.16}_{-0.1}$
GW190915_235702	$25.3^{+3.2}_{-2.7}$	$0.69^{+0.27}_{-0.27}$	$0.02^{+0.2}_{-0.25}$	$0.55^{+0.36}_{-0.39}$	$0.3^{+0.11}_{-0.1}$
GW190924_021846	$5.8^{+0.2}_{-0.2}$	$0.57^{+0.36}_{-0.37}$	$0.03^{+0.3}_{-0.09}$	$0.24^{+0.4}_{-0.18}$	$0.12^{+0.04}_{-0.04}$
GW190925_232845	$15.8^{+1.1}_{-1.0}$	$0.73^{+0.24}_{-0.34}$	$0.11^{+0.17}_{-0.14}$	$0.39^{+0.43}_{-0.29}$	$0.19^{+0.07}_{-0.07}$
GW190930_133541	$8.5^{+0.5}_{-0.5}$	$0.64^{+0.3}_{-0.45}$	$0.14^{+0.31}_{-0.15}$	$0.34^{+0.4}_{-0.24}$	$0.15^{+0.06}_{-0.06}$
GW191105_143521	$7.8^{+0.6}_{-0.4}$	$0.72^{+0.24}_{-0.31}$	$-0.02^{+0.13}_{-0.09}$	$0.3^{+0.45}_{-0.24}$	$0.23^{+0.07}_{-0.09}$
GW191109_010717	$47.5^{+9.6}_{-7.5}$	$0.73^{+0.21}_{-0.24}$	$-0.29^{+0.42}_{-0.31}$	$0.63^{+0.29}_{-0.37}$	$0.25^{+0.18}_{-0.12}$
GW191129_134029	$7.3^{+0.4}_{-0.3}$	$0.63^{+0.31}_{-0.29}$	$0.06^{+0.16}_{-0.08}$	$0.26^{+0.36}_{-0.19}$	$0.16^{+0.05}_{-0.06}$
GW191204_171526	$8.6^{+0.4}_{-0.3}$	$0.69^{+0.25}_{-0.26}$	$0.16^{+0.08}_{-0.05}$	$0.39^{+0.35}_{-0.26}$	$0.13^{+0.04}_{-0.05}$
GW191215_223052	$18.4^{+2.2}_{-1.7}$	$0.73^{+0.24}_{-0.27}$	$-0.04^{+0.17}_{-0.21}$	$0.5^{+0.37}_{-0.38}$	$0.35^{+0.13}_{-0.14}$
GW191216_213338	$8.3^{+0.2}_{-0.2}$	$0.64^{+0.31}_{-0.29}$	$0.11^{+0.13}_{-0.06}$	$0.23^{+0.35}_{-0.16}$	$0.07^{+0.02}_{-0.03}$
GW191222_033537	$33.8^{+7.1}_{-5.0}$	$0.79^{+0.18}_{-0.32}$	$-0.04^{+0.2}_{-0.25}$	$0.41^{+0.41}_{-0.32}$	$0.51^{+0.23}_{-0.26}$
GW191230_180458	$36.5^{+8.2}_{-5.6}$	$0.77^{+0.2}_{-0.34}$	$-0.05^{+0.26}_{-0.31}$	$0.52^{+0.38}_{-0.39}$	$0.69^{+0.26}_{-0.27}$
GW200112_155838	$27.4^{+2.6}_{-2.1}$	$0.81^{+0.17}_{-0.26}$	$0.06^{+0.15}_{-0.15}$	$0.39^{+0.39}_{-0.3}$	$0.24^{+0.07}_{-0.08}$
GW200128_022011	$32.0^{+7.5}_{-5.5}$	$0.8^{+0.18}_{-0.3}$	$0.12^{+0.24}_{-0.25}$	$0.57^{+0.34}_{-0.4}$	$0.56^{+0.28}_{-0.28}$
GW200129_065458	$27.2^{+2.1}_{-2.3}$	$0.85^{+0.12}_{-0.41}$	$0.11^{+0.11}_{-0.16}$	$0.52^{+0.42}_{-0.37}$	$0.18^{+0.05}_{-0.07}$
GW200202_154313	$7.5^{+0.2}_{-0.2}$	$0.72^{+0.24}_{-0.31}$	$0.04^{+0.13}_{-0.06}$	$0.28^{+0.4}_{-0.22}$	$0.09^{+0.03}_{-0.03}$
GW200208_130117	$27.7^{+3.6}_{-3.1}$	$0.73^{+0.23}_{-0.29}$	$-0.07^{+0.22}_{-0.27}$	$0.38^{+0.41}_{-0.29}$	$0.4^{+0.15}_{-0.14}$
GW200209_085452	$26.7^{+6.0}_{-4.2}$	$0.78^{+0.19}_{-0.31}$	$-0.12^{+0.24}_{-0.3}$	$0.51^{+0.39}_{-0.37}$	$0.57^{+0.25}_{-0.26}$
GW200219_094415	$27.6^{+5.6}_{-3.8}$	$0.77^{+0.21}_{-0.32}$	$-0.08^{+0.23}_{-0.35}$	$0.48^{+0.4}_{-0.35}$	$0.57^{+0.25}_{-0.22}$
GW200224_222234	$31.1^{+3.2}_{-2.6}$	$0.82^{+0.16}_{-0.26}$	$0.1^{+0.15}_{-0.15}$	$0.49^{+0.37}_{-0.36}$	$0.32^{+0.08}_{-0.11}$
GW200225_060421	$14.2^{+1.5}_{-1.4}$	$0.73^{+0.23}_{-0.28}$	$-0.12^{+0.17}_{-0.28}$	$0.53^{+0.34}_{-0.38}$	$0.22^{+0.09}_{-0.1}$
GW200302_015811	$23.4^{+4.7}_{-3.0}$	$0.53^{+0.36}_{-0.2}$	$0.01^{+0.25}_{-0.26}$	$0.37^{+0.45}_{-0.28}$	$0.28^{+0.16}_{-0.12}$
GW200311_115853	$26.6^{+2.4}_{-2.0}$	$0.82^{+0.16}_{-0.27}$	$-0.02^{+0.16}_{-0.2}$	$0.45^{+0.4}_{-0.35}$	$0.23^{+0.05}_{-0.07}$
GW200316_215756	$8.8^{+0.6}_{-0.6}$	$0.6^{+0.34}_{-0.38}$	$0.13^{+0.27}_{-0.1}$	$0.29^{+0.38}_{-0.2}$	$0.22^{+0.08}_{-0.08}$